Journal of The Electrochemical Society, **154** (3) B341-B351 (2007)
0013-4651/2007/154(3)/B341/11/$20.00 © The Electrochemical Society

A Multiphase Model for Cold Start of Polymer Electrolyte Fuel Cells

Leng Mao, Chao-Yang Wang,*,z and Yuichiro Tabuchi[a]

Electrochemical Engine Center and Department of Mechanical and Nuclear Engineering, The Pennsylvania State University, University Park, Pennsylvania 16802, USA

A multiphase and transient model is presented to describe transport and electrochemical processes with ice formation during startup of polymer electrolyte fuel cells (PEFCs) from subzero temperatures. The model accounts for ice/frost precipitation and growth in the cathode catalyst layer (CL) and gas diffusion layer, water transport at very low temperatures, heat transfer with phase transition, oxygen transport, electrochemical kinetics, and their mutual interactions. The governing equations of mass, momentum, species, heat, and charge transport under cold-start conditions are developed in a single-domain framework and solved by a finite-volume-based computational fluid-dynamics technique. Validated by extensive experimental data, this computational model is used to predict PEFC cold-start performance as well as to reveal 3D distributions of current density, temperature, membrane water content and ice fraction in the CL. Effects of startup current density and membrane thickness are numerically explored to illustrate the utility of the model.
 [DOI: 10.1149/1.2430651]

Manuscript submitted September 6, 2006; revised manuscript received October 27, 2006.
Available electronically January 19, 2007.

Self-startup of a polymer electrolyte fuel cell (PEFC) under extremely cold weather, known as "cold start," has emerged as a scientific challenge. It is recognized that water produced from the oxygen reduction reaction (ORR) forms ice or frost inside the cathode catalyst layer (CL) and gas diffusion layer (GDL) at subzero temperatures. The resulting ice not only plugs the pores of these layers, thus hindering oxygen transport, but also covers the reaction site, reducing the active electrochemical area (ECA). Both factors dramatically reduce fuel cell operating voltage under load, even causing shutdown of the cell. In a large-active-area PEFC, regions that are plugged by ice may then impose more stringent operating conditions on unplugged sections of the membrane electrode assembly (MEA); for example, current density in a partially blocked cell is redistributed to the remaining operable active areas. The increased local current density (and water production) exacerbates kinetic and transport deficiencies in remaining operating areas and further polarizes the cell in a cascading failure that may lead to cell voltage reversal and cell damage.

Earlier studies focused exclusively on MEA durability under freeze/thaw cycling between subzero and room temperatures.[1-3] No water production is involved during thermal cycling. Most recently, cold start of PEFCs under load, where water is produced from ORR, has been examined experimentally by Hishinuma et al.,[4] Oszcipok et al.,[5,6] Mao et al.,[7] Ge and Wang,[8] and Tajiri et al.[9] Hishinuma et al. found that self-startup without external heat assist was impossible from ambient temperatures below −5°C because the cathode exhaust, even with very large flowrates, cannot remove product water sufficiently to prevent ice formation in the catalyst layer and hence cell shutdown. Oszcipok et al.[5,6] revealed the importance of air flowrate during cold start and gas purge prior to cold start. Mao et al.[7] was among the first to study MEA degradation mechanisms resulting from cold start (i.e., in the presence of water production) and revealed interfacial delamination between the membrane and cathode catalyst layer after 110 cycles of cold start at 500 mA/cm^2 by transmission electron microscopy (TEM), but no such delamination was found in the same MEA from 110 cycles of cold start at 100 mA/cm^2. Using visualization images obtained from an operating PEFC, Ge and Wang[8] investigated liquid-water transport prior to freezing and ice/frost formation after freezing directly on the surface of the catalyst layer. Their work concluded that the freezing-point depression of water in the cathode CL is no greater than 2°C and plays a negligible role in cold-start theory and practice. The work of Tajiri et al.[9] developed a set of novel experimental protocols aimed at elucidating fundamentals of PEFC cold start, including a method of equilibrium purge using partially humidified gas for gas purge and isothermal cold start where the fuel cell plate temperature is kept constant at the ambient startup temperature and cumulative product water till cell shutdown is used to quantify the intrinsic cold-start performance.

On the basis of the experimental evidence, Mao and Wang[10] formulated a comprehensive theory of cold start from the principles of coupled water and heat transport with ice formation. Figure 1 schematically illustrates microscale ice formation and distribution in the cathode CL as a result of water production from ORR. The fraction of ice occupying open pores is dependent on the rate of product water diffused into the ionomeric membrane as well as transported into the GDL in the form of vapor-phase transport. Liquid-water transport out of the CL is found irrelevant in the cold-start problem unless the cell temperature closely approaches the freezing point (e.g., −2°C), in which situation water removal from the cathode CL is adequate and the fuel cell can operate indefinitely without ice formation inside the CL.

While the analytical model of Mao and Wang[10] addresses, for the first time, the important physics of coupled water and heat transport with ice formation, accurate prediction of PEFC cold start unfortunately requires 3D treatment because major phenomena governing cold start occur in all three dimensions. In the through-plane direction, water transport through the membrane at very low temperatures and vapor-phase transport of water between the CL and GDL are essential to a cold-start model. Heat transfer occurring primarily along the in-plane direction of the GDL between the channel and land determines the temperature difference between the CL and land. There is a dramatic impact on the ice-fraction evolution in the cathode CL if the local temperature in the CL is a few degrees higher than the land. Finally, along the flow direction, there may exist a nonuniform distribution of ice at the commencement of cold start, which may cause a portion of active-area to shut down due to ice plugging. Understanding how the local current density redistributes and the ice-blocked portion eventually resumes its operation after successful startup requires a 3D model.

The purpose of this work is to develop a 3D, multiphase, and transient model to predict PEFC cold-start behaviors. The model treats not only the interrelated transport phenomena of mass, momentum, species, charge, and heat, but also ice formation/melting, as well as its couplings with the transport and electrochemical processes. The multiphase cold-start model draws heavily upon three subareas of contemporary PEFC modeling for operations above

* Electrochemical Society Active Member.
[a] Permanent address: Nissan Motor Company Limited.
[z] E-mail: cxw31@psu.edu

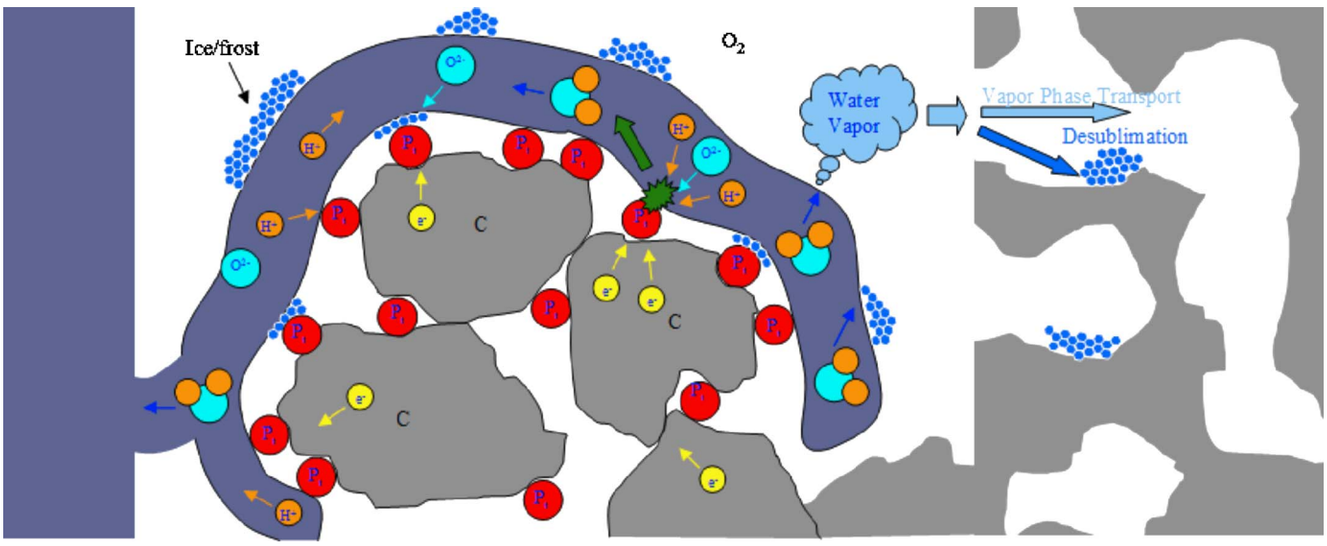

Figure 1. (Color online) Schematic of ice formation and distribution in the cathode catalyst layer.

freezing: water transport, heat transport, and transient phenomena. An extensive review of these three areas was provided recently by Wang.[11]

The present paper is organized as follows. The next section describes the multiphase 3D model for PEFC cold start as well as its solution by computational fluid dynamics (CFD), and the Results and Discussion section presents experimental validation of this model as well as parametric studies of current density and membrane thickness effects on PEFC cold-start performance. The final section summarizes the conclusions and indicates future work.

Multiphase Model

In this section, a multiphase transient model of PEFC cold start is formulated using a single-domain approach so as to be amenable to 3D simulations for industrial-scale fuel cells. The PEFC system at subzero temperatures is considered to consist of water vapor in the gas phase and ice/frost, assuming instantaneous desublimation of water from supersaturated vapor. We have excluded the existence of liquid water in this work, which is indeed a good approximation in the temperature range from −30 to approximately −2°C, according to the visualization study of Ge and Wang.[8] Between −2°C and the freezing point, the PEFC startup should not be an issue. However, in future work where post-cold-start events are of special interest, one may include liquid water as the third phase in this multiphase model. Other model assumptions are (*i*) negligible gravity effect, (*ii*) ideal gas mixtures, (*iii*) incompressible gas due to small pressure gradients, (*iv*) laminar flow due to small flow velocities, and (*v*) isotropic and homogeneous porous layers characterized by an effective porosity and permeability.

Based on the multiphase approach, PEFC cold-start operation can be described by mass, momentum, species, charge, and energy conservation principles with a proper account of ice formation and its interactions with transport phenomena and ORR. The mass and momentum equations determine the flow field. To ensure flux continuity at the interface between the porous GDL and gas channel, superficial fluid velocity vector $\vec{u}$ is chosen for the mass and momentum equations. Thus, the mass-conservation equation in the cold-start model reads as

$$\frac{\partial(\varepsilon_s \rho_s)}{\partial t} + \frac{\partial(\varepsilon\rho)}{\partial t} + \nabla \cdot (\rho\vec{u}) = S_m \qquad [1]$$

where ρ is the gas-mixture density, ρ_s the density of solid ice, and ε the volume fraction of open pores and can be expressed as $\varepsilon = \varepsilon_0(1 - s)$, with ε_0 being the initial porosity of a porous layer and s the ice fraction in the pore spaces defined as the volume fraction of ice to void space in the CL, i.e., $s = V_{\text{ice}}/V_{\text{void}}$. The volume fraction of open pores is not a constant but a variable during cold start due to ice formation. Similarly, the ice-volume fraction can be expressed as $\varepsilon_s = \varepsilon_0 s$. The mass source/sink term S_m accounts for mass consumption or creation from an electrochemical reaction and water-transport fluxes through the membrane between the anode and cathode. Thus, in the anode CL this term includes hydrogen oxidation and water transport through the membrane by diffusion and electro-osmotic drag, expressed as

$$S_{m,a} = -M_{\text{H}_2}\frac{j}{2F} + M_w\left[\nabla \cdot (D_{w,m} \nabla C_w) - \nabla \cdot \left(n_d \frac{i_e}{F}\right)\right] \qquad [2]$$

In the cathode, the mass-source term includes oxygen consumption and water production from ORR as well as the water transport through the membrane, shown as follows

$$S_{m,c} = M_{\text{O}_2}\frac{j}{4F} - M_{\text{H}_2\text{O}}\frac{j}{2F} + M_w\left[\nabla \cdot (D_{w,m} \nabla C_w) - \nabla \cdot \left(n_d \frac{i_e}{F}\right)\right] \qquad [3]$$

More details on the derivation of Eq. 2 and 3 can be found in Wang and Wang.[12]

To be valid in both porous layer and gas channel, the momentum equation can be generalized as

$$\frac{1}{\varepsilon}\left[\frac{\partial(\rho\vec{u})}{\partial t} + \frac{1}{\varepsilon}\nabla \cdot (\rho\vec{u}\vec{u})\right] = \nabla \cdot (\mu_{\text{eff}} \nabla \vec{u}) - \nabla p + \rho\vec{g} - \frac{\mu}{K}\vec{u} \qquad [4]$$

The additional term, $(\mu/K)\vec{u}$, represents the drag force exerted on the fluid from the solid matrix that is proportional to fluid viscosity μ and velocity $\vec{u}$. This term vanishes in the gas channel as the permeability K goes to infinity. Within porous layers, this equation reduces to Darcy's law with a variable permeability

$$\vec{u} = -\frac{K}{\mu}\nabla p \qquad [5]$$

In the presence of ice formation, part of the available pore space is occupied by solid ice, thus the cross-sectional area available for fluid flow is less than the total pore space. This phenomenon can be modeled by the concept of relative permeability k_r, which defines the ratio of the actual permeability for flow at a given ice fraction to the intrinsic permeability of the porous medium. The same concept

is widely used in the modeling of electrode flooding.[13] In this work, the fluid relative permeability is assumed to be proportional to the cube of ice fraction. That is

$$K = (1 - s)^3 K_0 \quad [6]$$

where K_0 is the intrinsic permeability of a porous medium in the absence of ice.

The generalized species equation expressed in the following form can be solved to obtain hydrogen, oxygen, and water distributions

$$\varepsilon \frac{\partial C^i}{\partial t} + \nabla \cdot (\vec{u} C^i) = \nabla \cdot (D^i_{\text{eff}} \nabla C^i) + S^i_c \quad [7]$$

where the superscript "i" denotes species i. The effective species diffusion coefficient in the above equation is modified via Bruggeman correlation to account for the effects of porosity and tortuosity of porous layers,[14] namely

$$D^i_{\text{eff}} = \varepsilon^{1.5} D^i = [\varepsilon_0 (1 - s)]^{1.5} D^i \quad [8]$$

For hydrogen and oxygen, the term S^i_c represents a source/sink in the CL arising from electrochemical reactions, which is proportional to the transfer current density, i.e.

$$S^i_c = - \frac{s^i j}{nF} \quad [9]$$

where s^i is the stoichiometry coefficient of species i in the anodic or cathodic reaction and n the number of electrons transferred.

For water transport the source term $S^{H_2O}_c$ includes not only production water from ORR but also the electro-osmotic drag and phase transition of water

$$S^{H_2O}_c = - \frac{s^{H_2O} j}{nF} - \nabla \cdot \left(\frac{n_d}{F} I_e \right) + \dot{q}^{H_2O}_{sg} \quad [10]$$

The electro-osmotic drag coefficient n_d in the above equation is taken to be unity for $0 < \lambda < 14$ in the present study. Under the assumption of instantaneous desublimation, the ice formation rate $\dot{q}^{H_2O}_{sg}$ can be determined from the water-conservation equation, Eq. 7, with the local water concentration fixed at $C^{H_2O}_{sat}$, following the large-source technique of Voller.[15] Physically, this means that the extra water in the gas phase beyond the saturation level is turned into ice instantly, accumulating locally. Similarly, the ice melting rate, occurring when the local temperature reaches the freezing point, is determined from the heat-balance equation, with the local temperature fixed at the freezing point until all the ice melts completely.

As pointed out by Wang and Wang,[16] The generalized species equation, Eq. 7, encompasses the water-transport equations in the membrane and CL. For example, in the membrane region, Eq. 7 reduces to

$$\varepsilon_m \frac{\partial C^{H_2O}_m}{\partial t} = \nabla \cdot (D^{H_2O}_m \nabla C^{H_2O}_m) - \nabla \cdot \left(\frac{n_d}{F} I_e \right) \quad [11]$$

with the fluid velocity assumed to be zero in the membrane. The above equation precisely describes two important modes of water transport through the ionomeric membrane, electro-osmotic drag and molecular diffusion. In this equation, ε_m is the ionomer fraction in the membrane, taken as unity in the present work. The water molar concentration in the membrane, $C^{H_2O}_m$, is defined as

$$C^{H_2O}_m = \frac{\rho_m \lambda}{EW} \quad [12]$$

where ρ_m and EW are the density and equivalent weight of the membrane, respectively. The water content, λ, is defined as the number of water molecules per sulfonic acid group. The one-to-one relationship between the membrane water content and water activity of the surrounding gas is given by the water uptake curve[17]

$$\lambda = 0.043 + 17.18a - 39.85a^2 + 36.0a^3 \quad \text{for } 0 < a \leqslant 1 \quad [13]$$

where water activity is defined as

$$a = \frac{C^{H_2O}}{C^{H_2O}_{sat}} = \frac{C^{H_2O} RT}{p_{sat}} \quad [14]$$

The saturation pressure of water vapor over ice p_{sat} is calculated by the Clapeyron–Clausius equation

$$p_{sat}(T) = 611.3 \exp\left[\frac{h_{sg}}{R} \left(\frac{1}{273.15} - \frac{1}{T} \right) \right] \quad [15]$$

where the saturation pressure and latent heat of sublimation h_{sg} at the freezing point are 611.3 Pa and 2834.5 kJ/kg, respectively. Equation 15 is also in perfect agreement with the Goff Gratch equation presented in the Smithsonian Meteorological Tables.[18] Note that in the present model, the maximum water content in the membrane stays at 14, as water activity in the gas cannot go beyond unity.

Within the catalyst layer, the generalized water transport equation, Eq. 7, must include water transport through both the gas and ionomer phases. Therefore, the conservation equation is written as

$$\varepsilon \frac{\partial C^{H_2O}}{\partial t} + \varepsilon_m \frac{\partial C^{H_2O}_m}{\partial t} + \nabla \cdot (\vec{\mathbf{u}} C^{H_2O}) = \nabla \cdot (D^{H_2O}_{g,\text{eff}} \nabla C^{H_2O}_m) + S^{H_2O}_c \quad [16]$$

where ε_m stands for the ionomer fraction in the CL. The first two terms on the left represent the rate of water storage in the gas and ionomer phases, respectively. Assuming thermodynamic equilibrium of water between the gas and ionomer phases, the above equation can be rearranged into the same form as Eq. 7 with an effective factor, ε^{eff}, defined as

$$\varepsilon^{\text{eff}} = \varepsilon + \varepsilon_m \frac{dC^{H_2O}_m}{dC^{H_2O}} = \varepsilon + \varepsilon_m \frac{1}{EW} \frac{RT}{p_{sat}} \left(\rho_m + \lambda \frac{d\rho_m}{d\lambda} \right) \frac{d\lambda}{da} \quad [17]$$

This effective factor is on the order of 10^2–10^3 for water activity $a \leqslant 1$, signifying that the majority of water storage is in the ionomers.

The conservation equation for proton transport is solved throughout the MEA, which can be written as

$$\nabla \cdot (\kappa^{\text{eff}}_e \nabla \phi_e) + j = 0 \quad [18]$$

where ϕ_e denotes the electrolyte phase potential and κ^{eff}_e the effective proton conductivity of ionomers, modified via Bruggeman correlation to account for the ionomer volume fraction and tortuosity effect in the CL. Following Springer et al.,[17] the intrinsic proton conductivity of electrolyte has been correlated with water content and temperature based on the conductivity data measured by Tajiri et al.[9] for the temperature between 0 and −30°C and water content range between 2.4 and 14. This correlation was first presented by Mao et al.,[7] as given by

$$\kappa_e = \exp\left[2222 \left(\frac{1}{303} - \frac{1}{T} \right) \right] (0.005139\lambda - 0.00326) \text{ [S/cm]} \quad [19]$$

Note that the activation energy for proton conduction changes from 2.52 kcal/mol in the original Springer's formula to 4.42 kcal/mol (i.e., $E_a/R = 2222$ K) due to the different temperature ranges involved and different membranes (i.e., Nafion for Springer's correlation vs Gore–Select membranes for Eq. 19).

Electron transport is also considered in the present cold-start model, as this conservation equation must be solved in order to impose the constant current-density boundary condition commonly used in PEFC operation. The electron conservation equation can be written as

Table I. Summary of governing equations.

Continuity	$\frac{\partial(\varepsilon_s\rho_s)}{\partial t} + \frac{\partial(\varepsilon\rho)}{\partial t} + \nabla \cdot (\rho\vec{u}) = S_m$
Momentum	$\frac{1}{\varepsilon}\left[\frac{\partial(\rho\vec{u})}{\partial t} + \frac{1}{\varepsilon}\nabla \cdot (\rho\vec{u}\vec{u})\right] = \nabla \cdot (\mu_{\text{eff}}\nabla\vec{u}) - \nabla p + \rho\vec{g} - \frac{\mu}{K}\vec{u}$
Species	$\varepsilon\frac{\partial C^i}{\partial t} + \nabla \cdot (\vec{u}C^i) = \nabla \cdot (D^i_{\text{eff}}\nabla C^i) + S^i_c$
Charge	$\nabla \cdot (\kappa^{\text{eff}}_e \nabla \phi_e) + j = 0 \qquad \nabla \cdot (\sigma^{\text{eff}}_s \nabla \phi_s) - j = 0$
Energy	$[(\varepsilon\rho C_p)_s + (\varepsilon\rho C_p)_g]\frac{\partial T}{\partial t} + \nabla \cdot [(\varepsilon\rho C_p)_g\vec{u}T] = \nabla \cdot (k_{\text{eff}}\nabla T) + S_T$
Electrochemical Reactions:	$\Sigma_i s_i M_i^z = ne^-$ In PEFC, there are: (Anode) H_2–$2H^+ = 2e^-$ (Cathode) $2H_2O$–O_2–$4H^+ = 4e^-$

$$\nabla \cdot (\sigma^{\text{eff}}_s \nabla \phi_s) - j = 0 \quad [20]$$

where ϕ_s denotes the electron phase potential and σ^{eff}_s the effective electronic conductivity.

The local temperature directly determines water fluxes via membrane—or vapor-phase transport and ice formation in the CL, thereby critically impacting the fate of PEFC startup. To obtain the temperature distribution, the energy conservation equation in the following form is solved

$$[(\varepsilon\rho c_p)_s + (\varepsilon\rho c_p)_g]\frac{\partial T}{\partial t} + \nabla \cdot [(\varepsilon\rho c_p)_g\vec{\mathbf{u}}T] = \nabla \cdot (k_{\text{eff}}\nabla T) + S_T \quad [21]$$

where the first two terms on the left side stand for thermal energy accumulation with time in the solid phase and fluid, respectively. The third and fourth terms denote the fluid convection and conduction through the fluid-porous matrix composite. The last term is heat generation that includes the entropic heat and irreversible heat of electrochemical reactions, Joule heat as well as latent heat due to water freezing or melting. That is[19]

$$S_T = j\left(\eta - T\frac{\partial U_o}{\partial T}\right) + \frac{i_e^2}{\kappa^{\text{eff}}_e} + \dot{q}^{\text{H}_2\text{O}}_{\text{sg}}h_{\text{sg}} \quad [22]$$

where $\dot{q}^{\text{H}_2\text{O}}_{\text{sg}}$ is the phase change rate per unit of volume (mol/m^3 s). The total heat source is reduced to Joule heating only in the membrane region and latent heat of sublimation only in the GDL, respectively. Under normal operating conditions, the design goal is to minimize waste heat generation to attain high energy-conversion efficiency, while during cold start waste heat is desired to warm up the fuel cell for successful and fast startup.

The electrochemical-reaction kinetics is generally described by the Butler–Volmer equation. The anode exhibits facile electrokinetics and hence a low surface overpotential, therefore it can be expressed by a linear kinetic equation

$$j_a = ai^{\text{ref}}_{0,a}\left(\frac{C^{\text{H}_2}}{C^{\text{H}_2}_{\text{ref}}}\right)^{1/2}\left(\frac{\alpha_a + \alpha_c}{RT}F\eta\right) \quad [23]$$

The cathode has relatively slow kinetics with higher surface overpotential so that it is described by Tafel kinetics

$$j_c = ai^{\text{ref}}_{0,c}\frac{C^{\text{O}_2}}{C^{\text{O}_2}_{\text{ref}}}\exp\left(-\frac{\alpha_c}{RT}F\eta\right) \quad [24]$$

The surface overpotential in the above kinetic equations is defined as

$$\eta = \phi_s - \phi_e - U_o \quad [25]$$

where U_o stands for the thermodynamic equilibrium potential of an electrochemical reaction, which is zero on the anode but a function of temperature at the cathode

$$U_o^{\text{anode}} = 0$$

$$U_o^{\text{cathode}} = 1.23 - 9.0 \times 10^{-4}(T - 298.15) \quad [26]$$

It is not precisely known how solid ice blocks the access of electrons, protons, and reactants to active reaction sites. In this work, a linear reduction of ECA with the ice fraction is assumed, that is

$$a = (1 - s)a_o \quad [27]$$

where a_o is the total ECA per unit of CL volume. Hence, a_o is a function of Pt loading and the CL thickness.

The resulting set of governing equations is summarized in Table I. The conservation equations are discretized using a finite-volume method and solved with commercially flow solver, Fluent, by customizing its user defined functions (UDF). The fully implicit scheme is used in order to maximize the time step and reduce the computational time. An independent study of both mesh-density and time-step has been performed to ensure adequate spatial and time resolution.[10] The transient, three-dimensional simulation of a typical cold-start case shown in the next section requires roughly 20 h on a single-processor PC.

Results and Discussion

Experimental validation.— The multiphase model described in the preceding section has been validated against an extensive set of experimental data[9] under various cold-start conditions (varying purge practice, startup current density, and temperature) and with different MEA designs (various membrane thickness). All these experiments were conducted under the constant temperature boundary condition, that is, the land surface temperature is kept constant at the ambient startup temperature throughout the cold start, an experimental protocol termed as temporally isothermal cold start.[9] Under this thermal boundary condition, the temperature throughout the fuel cell varies much less with time than with location; there is spatial gradient in the temperature from the CL to the land through the GDL. Therefore, all these experiments resulted in shutdown; however, the cumulative product water created prior to cell shutdown provides a quantitative index to measure intrinsic cold-start capability of the MEA, independent of the cell fixture and its thermal mass. A detailed discussion of isothermal cold-start experiments can be found in Tajiri et al.[9] All calculations presented in this work are concerned

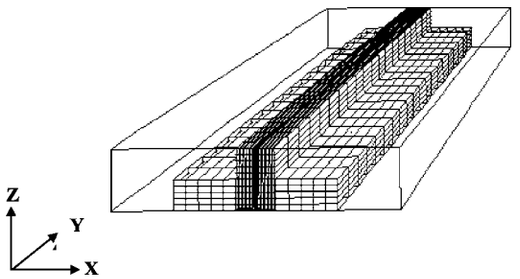

Figure 2. Geometry and numerical mesh of a single-channel PEFC.

with isothermal cold start. Voltage curves and cumulative product water measured from these experiments are used for model validation. Exploration of nonisothermal cold start is documented elsewhere.[10]

Validation data were obtained from a 25 cm^2 cell with parallel channel flowfield on both the anode and cathode. Due to symmetry, a single-channel geometry shown in Fig. 2 is sufficient for 3D numerical simulation of the cold-start experiments. The geometric parameters and operating conditions are listed in Table II, with the electrochemical properties and transport parameters used in simulations given in Table III.

The initial temperature through an entire cell is uniform and set the same as the startup ambient temperature. Dry gases are used for both anode and cathode inlets with the flow stoichiometric ratio of 2 under the applied current density. The initial water distribution in the cell is critically important for cold-start performance. This condition is affected by two types of gas purge in the validation experiments: equilibrium purge and dry-gas purge. In equilibrium purge, purge gas of controlled relative humidity is applied for several hours as described in detail by Tajiri et al.,[9] no initial ice exists throughout the cell prior to cold start, and the initial membrane water content uniformly corresponds to the relative humidity of purge gas. In contrast, dry purge employs dry gas to purge the cell for short intervals, usually on the order of 30–60 s. In this case, the initial ice fraction is assumed to be 30% in the cathode CL, and initial membrane water content λ_o is obtained from the measured membrane resistance after dry-gas purge and cool-down via the proton-conductivity formula given in Eq. 19.

Table II. Geometric parameters and operating conditions.

Description	Unit	Value
Geometric parameters		
Anode/cathode gas channel depth/width	mm	1
Land width	mm	1
Cell length	mm	100
Anode/cathode GDL Thickness	μm	300
Anode/cathode CL Thickness	μm	10
Membrane thickness	μm	30
Material properties		
Permeability of anode/cathode GDL	m^2	1.0×10^{-12}
Permeability of anode/cathode CL	m^2	1.0×10^{-13}
Anode/cathode GDL porosity		0.6
Anode/cathode CL porosity		0.5
Ionomer volume fraction in CL		0.15
Equivalent weight of ionomers	kg/mol	1.1
Dry density of membrane	kg/m^3	1.98×10^3
Operating conditions		
Baseline current density (with equilibrium purge)	mA/cm^2	40
Baseline current density (with short purge)	mA/cm^2	100
Anode stoichoimetry		2.0
Cathode stoichoimetry		2.0

Table III. Electrochemical and transport properties.

Description	Unit	Value
Electrochemical kinetics		
Anode reference exchange current density	A/m^3	10^9
Cathode reference exchange current density	A/m^3	10^4
Faraday constant	C/mol	96487
Species transport parameters		
H_2 diffusivity	m^2/s	8.67×10^{-5}
O_2 diffusivity	m^2/s	1.53×10^{-5}
H_2O diffusivity at anode	m^2/s	8.67×10^{-5}
H_2O diffusivity at cathode	m^2/s	1.79×10^{-5}
Anode gas viscosity	m^2/s	9.88×10^{-6}
Cathode gas viscosity	m^2/s	1.36×10^{-5}
Thermal properties		
H_2 thermal conductivity	W/m K	0.170
O_2 thermal conductivity	W/m K	0.024
N_2 thermal conductivity	W/m K	0.024
H_2O vapor thermal conductivity	W/m K	0.024
Anode/cathode GDL conductivity	W/m K	1.2
Anode/cathode CL conductivity	W/m K	1.5
Membrane thermal conductivity	W/m K	0.95
Anode/cathode bipolar plate thermal conductivity	W/m K	20.0
H_2 density	kg/m^3	0.09
O_2 density	kg/m^3	1.4
N_2 density	kg/m^3	1.2
H_2O vapor density	kg/m^3	0.8
H_2 specific heat	J/kg K	14400
O_2 specific heat	J/kg K	917
N_2 specific heat	J/kg K	1041
H_2O vapor specific heat	J/kg K	2000
Anode/cathode GDL heat capacity	$J/K\ m^3$	5.68×10^5
Anode/cathode CL heat capacity	$J/K\ m^3$	1.69×10^6
Membrane heat capacity	$J/K\ m^3$	1.65×10^6
Anode/cathode bipolar plate heat capacity	$J/K\ m^3$	1.57×10^6
Latent heat of sublimation	J/mol	5.1×10^{-4}
Electronic conductivities		
Anode/cathode GDL	S/m	300
Anode/cathode bipolar plate	S/m	20000

For the sake of brevity, only one representative model validation case (out of 40 experiments) is fully presented here. In this case, the fuel cell was purged with 75% relative humidity (RH) gas for several hours until all liquid water was removed from the cell and the membrane reached thermodynamic equilibrium with the purge gas RH. The cell was subsequently cooled to −20°C and started up from this temperature at 40 mA/cm^2. The simulated voltage curve is compared with the experimental data in Fig. 3. Note that a brief initial period of the current linearly ramping up to 40 mA/cm^2 in the experiment is due to convenience of operation, with negligible consequence on the cold-start physics of interest here. The simulation uses a stepwise current density and starts from the midpoint of this linear ramp period so as to conserve the total charge capacity. As can be seen from Fig. 3, the predicted and measured cell voltages match quite well in the first 140 s. Then, the simulated voltage drops suddenly at around 210 s after startup, while the voltage in the experiment drops more gradually. The overall trend of voltage dropdown due to ice formation in the cathode CL is consistent between the simulation and experiment. Also, predicted and measured cumulative product water agree favorably (0.82 vs 0.85 mg/cm^2). However, there is still room to improve the predicted shape of voltage dropdown, which is linked strongly to the ice morphology and surface coverage of ECA. Further investigation of the microscale distribution and morphology of frozen ice in the cathode CL is ongoing.

A comparison of predicted and measured cumulative product water for all 40 experiments is summarized in Fig. 4. The present

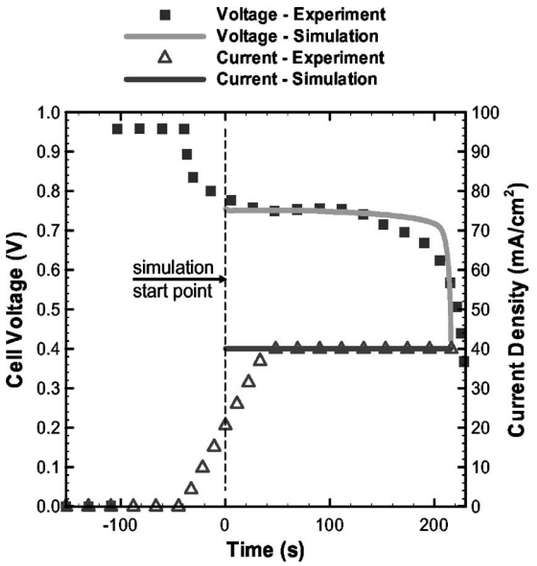

Figure 3. Experimental validation of discharge curve during cold start from −20°C at 40 mA/cm^2, where the experimental data are taken from Ref. 9.

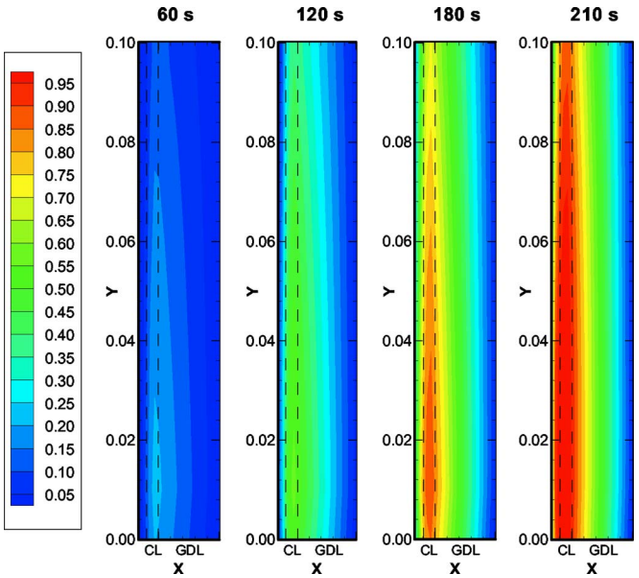

Figure 5. (Color online) Ice-fraction evolution in the cathode catalyst layer in the X–Y plane.

multiphase model is able to achieve ±20% accuracy, except for a few data points, over a wide range of cold-start conditions and fuel cell designs.

3D simulation results.— To shed light on the fundamentals of PEFC cold start, detailed distributions of ice fraction, temperature, current density, and membrane water content as predicted by the multiphase model in this subsection are presented here for the above-described validation case. Figures 5-7 display the ice-fraction evolution in the cathode CL during startup in various planes. The ice-fraction contours in the CL and GDL along the through-plane and flow directions are shown in Fig. 5 at various time instants. Upon startup, the ice fraction increases first in the cathode CL and then propagates into the GDL region next to the CL. With the assumption of instantaneous desublimation, ice formation in the CL is mainly determined by local water production. Along the flow direction, local current density decreases as a result of oxygen depletion. Therefore, the ice fraction grows faster near the inlet during most periods of cold start. The maximum ice fraction occurs at a small distance from the inlet where the dry inlet gas becomes saturated, leading to the onset of ice precipitation. In the very late stage of cold start, excessive ice formation ($s > 0.9$) inside the cathode CL shuts down the inlet region, thereby shifting both the current-density distribution and ice growth rate towards the downstream. When the outlet region is also shut down by ice formation in the CL, the cell voltage drops sharply, signifying the end of cold start at 210 s, as seen from Fig. 5 and 3.

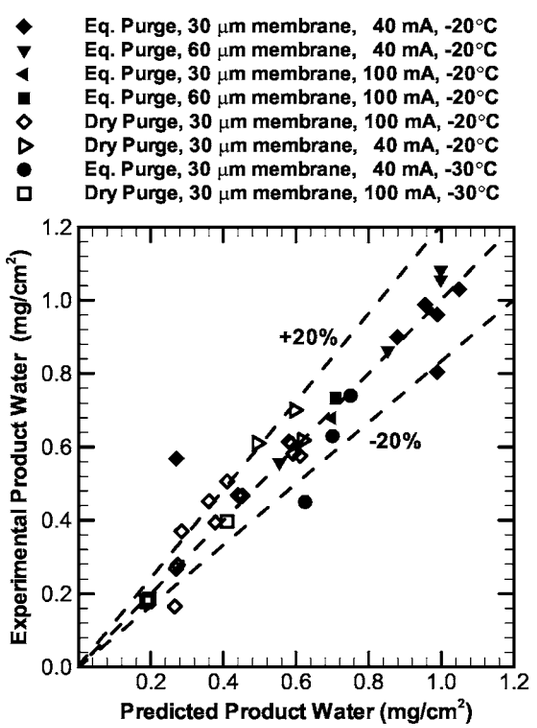

Figure 4. Experimental validation of cumulative product water under various cold-start conditions, with the experimental data taken from Ref. 9.

Ice growth in the cathode CL is shown in Fig. 6 at three flow cross sections: near the inlet, in the middle, and near the outlet. Each cross section includes half of the channel area (bottom) and half of the land area (top) in the Z-direction, with X-direction denoting the through-plane direction. The four groups correspond to four time instants of the startup. By comparing the three contour plots at each time instant, it is apparent that the ice in the CL always evolves faster at the inlet and subsequently propagates towards the outlet. However, by comparing the same cross section across four time instants, the ice fraction initially grows faster near the inlet, while at the late stage ice growth accelerates in the middle and near the outlet after excessive ice already formed at the inlet. Along the in-plane direction, the upper part under the land has a slightly higher ice fraction because the local temperature is lower. Along the through-plane direction, the highest ice fraction does not occur at the CL/membrane interface but towards the CL/GDL interface. During cold start, the PEFC operates at a very low current density, and therefore the oxygen transport through the CL is not limiting, while proton transport through ionomers is severely limited due to low proton conductivity at very low temperatures and low water content. Consequently, the local transfer current density is higher near the membrane than near the GDL until the oxygen transport becomes substantially limited by excessive ice formation. In spite of the higher water production rate near the membrane, the rate of ice formation there is slower, due mainly to water absorption by the membrane.

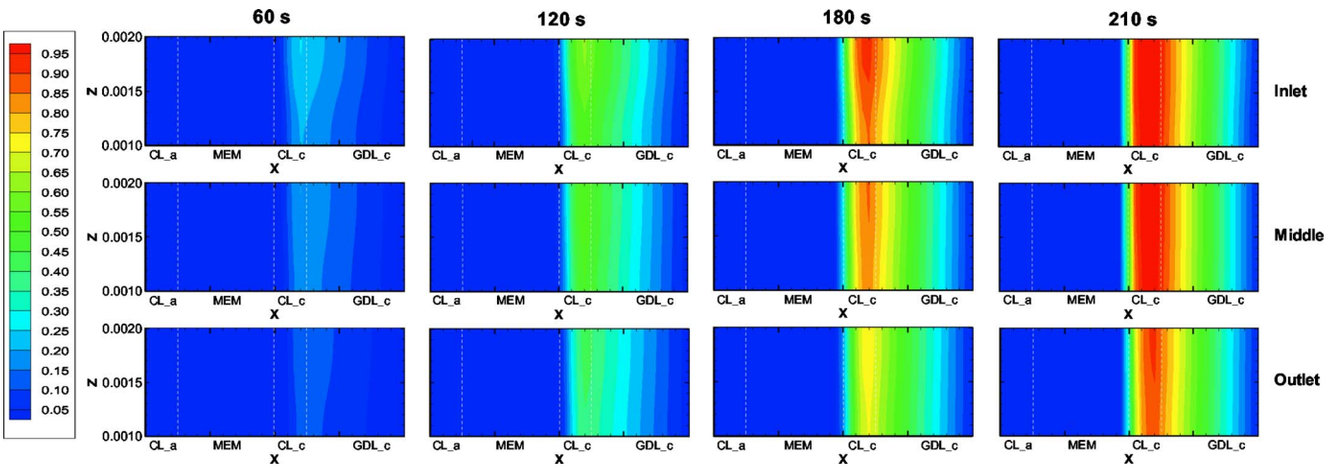

Figure 6. (Color online) Ice-fraction evolution in the cathode catalyst layer in the *X*–*Z* plane.

Faster ice growth near the CL/GDL interface is undesirable as the ice-sheet formed at the front side of the electrode blocks oxygen transport and causes premature cell shutdown before the entire CL is filled with ice.

Figure 7 depicts the ice-fraction contours at the center of the cathode CL. At 180 s into discharge, it is clearly seen that ice fraction decreases from the inlet towards the outlet, with the ice fraction at the inlet reaching the shutdown threshold, i.e., $s > 0.9$. Thereafter, the local current density shifts towards the outlet, filling up the cathode CL in the middle and then in the outlet region. At 210 s, the entire fuel cell CL is filled with ice, causing cell shutdown. Again, it can be seen from Fig. 7 that ice grows more underneath the land due to lower local temperature.

Directly influenced by ice formation, the current-density distribution at the center of the membrane is shown in Fig. 8. The average current density applied in the simulation is 40 mA/cm^2 or 400 A/m^2. In the early and middle stages of cold start with little ice formation, the current density is generally uniform. Only at the moment close to cell shutdown (i.e., 210 s) does the current density in the first half of the fuel cell fall below the average value due to ice blockage, while the local current density in the second half towards the outlet rises. There is a small region near the inlet underneath the channel area where local current density remains high due to slow ice growth resulting from water uptake by the dry inlet gas.

The water-content distribution at the membrane center is shown in Fig. 9. In general, the membrane water content increases with further discharge due to diffusion of product water into the membrane. However, the water content is far from the maximum value due to sluggish water diffusion through the membrane at −20°C. In the intermediate stage of cold start (between 120 and 180 s), the membrane water content slightly increases along the flow direction as the cathode gas becomes saturated with water vapor. At the end of cold start (210 s), there exists a region of low water content in the midsection of the fuel cell, as seen in the last contour plot. Here, the local current density is greatest as the inlet portion of the fuel cell is

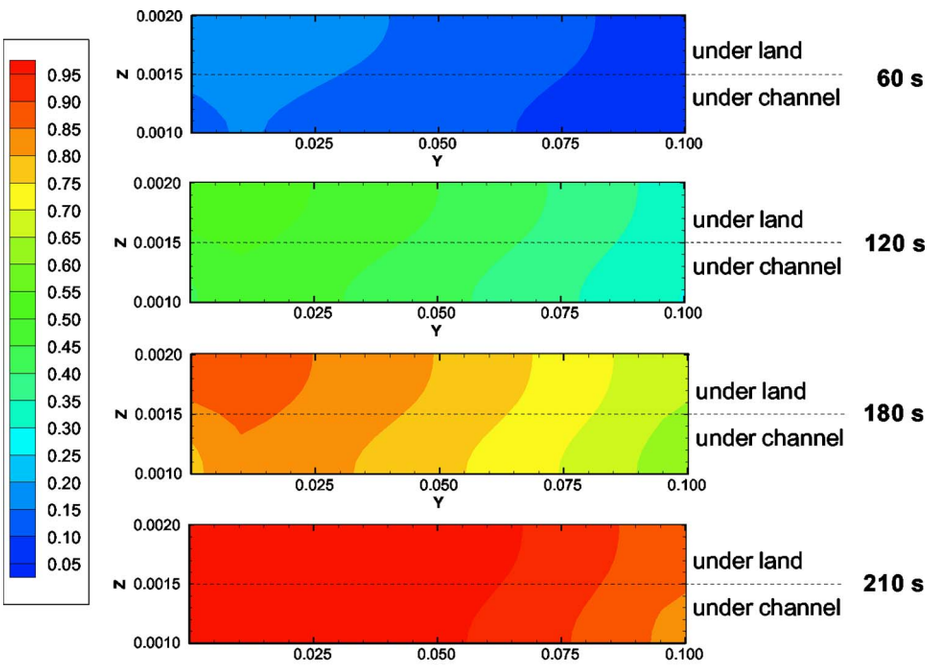

Figure 7. (Color online) Ice-fraction evolution in the cathode catalyst layer in the *Y*–*Z* plane.

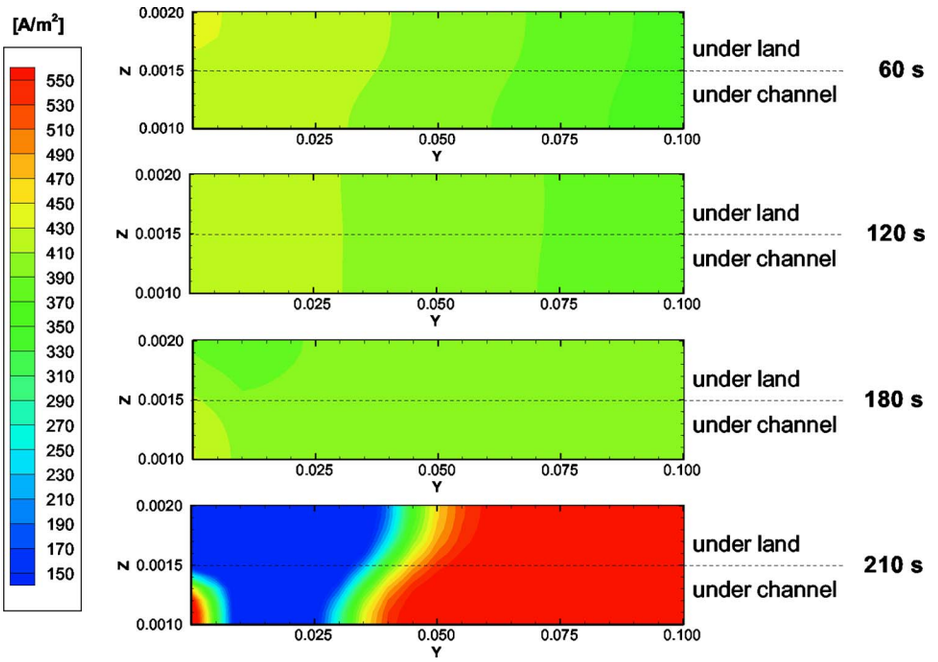

Figure 8. (Color online) Evolution of current-density distribution in the *Y–Z* plane at the center of the membrane.

shut down by ice blockage and the reaction front is pushed to the midsection. The high local current density results in enhanced electro-osmotic drag, thereby reducing the water content at the center of the membrane.

The temperature contours in the three flow cross sections are shown in Fig. 10. Note that the land surface is kept at the startup temperature (i.e., isothermal cold start). Thus, the only thermal gradient occurs in the GDL along the in-plane direction from channel to land. This spatial temperature difference is proportional to the heat generation rate (or current density) and inversely proportional to the GDL thermal conductivity. Due to the small current density applied in this simulation case, i.e., 40 mA/cm^2, the temperature difference is only ~0.3°C under the common GDL thermal conductivity of 1.2 W/m K (see Fig. 10). If one would engineer the GDL thermal conductivity or operating conditions to result in a temperature difference between the CL and land of 2–3°C, ice formation in the cathode CL would be significantly suppressed, thus improving cold-start performance.

Current-density effect.— The effect of the startup current density is numerically explored using the multiphase cold-start model. Figure 11 displays cumulative product water as a function of initial

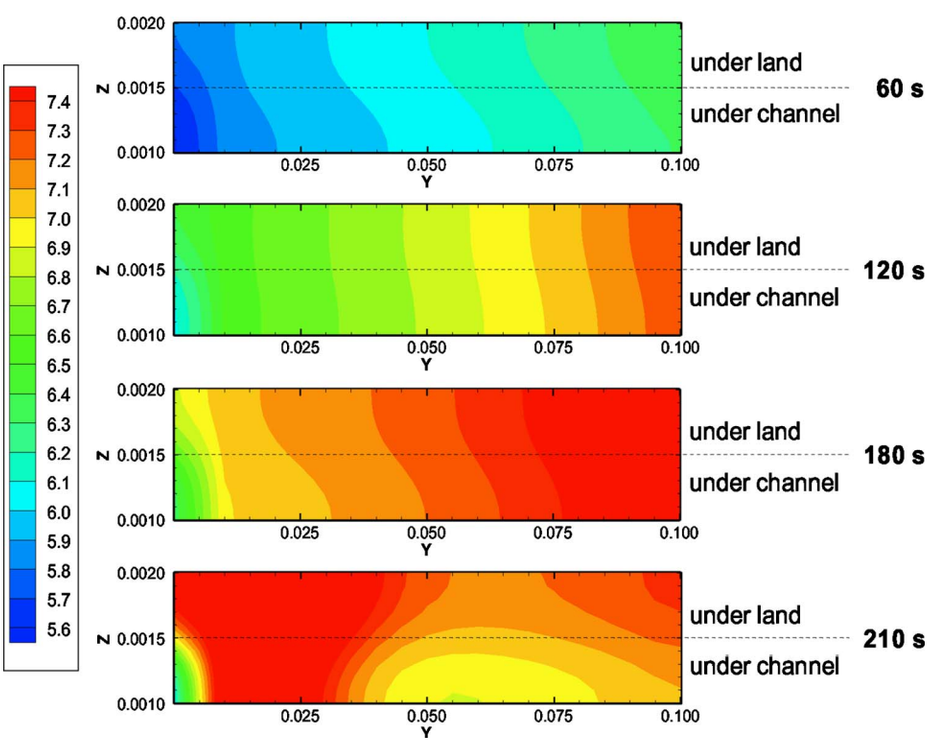

Figure 9. (Color online) Evolution of water-content distribution in the *Y–Z* plane at the center of the membrane.

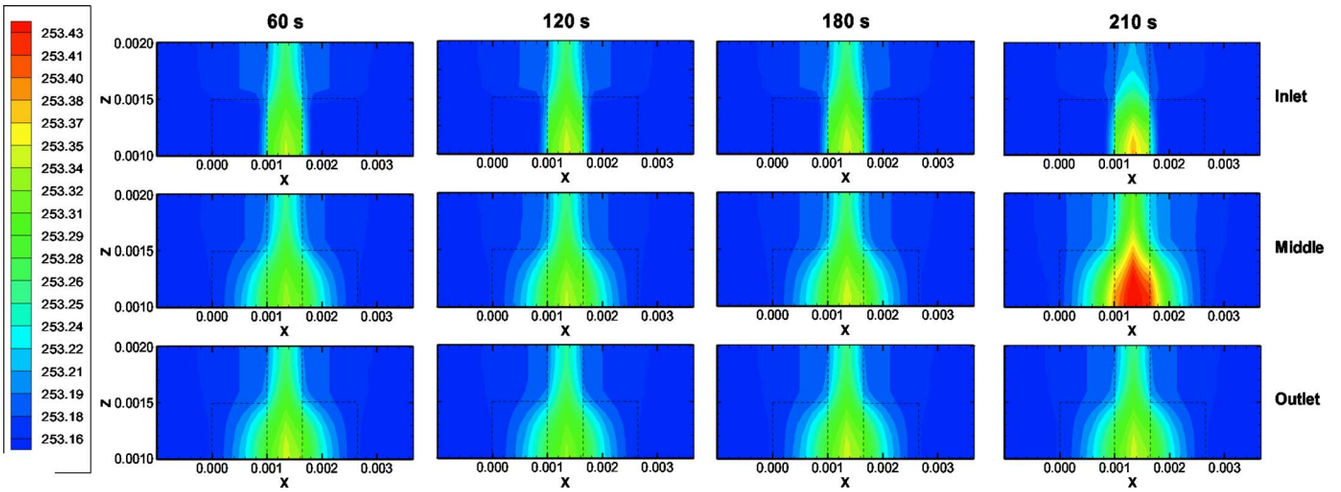

Figure 10. (Color online) Temperature contours in the *X*–*Z* plane.

membrane water uptake potential at two current densities. Here, the water uptake potential is defined as the difference between the membrane fully hydrated state and initial value effected by gas purge.[9,10] Because water storage in a partially dry membrane is an important mechanism to divert product water so as to alleviate ice formation in the cathode CL, there is a nonlinear relationship between the product water achievable in cold-start and the water uptake potential in the membrane, as can be seen from Fig. 11 and also as discussed in length by Tajiri et al.[9] and Mao and Wang.[10] Further, Fig. 11 shows a significant current-density effect. Under equivalent cumulative product water, operation at lower current density not only offers much more operable time to enhance water diffusion in the membrane but also retards ice accumulation in the CL, thus providing even more time for water storage in the membrane before cell shutdown. This can be more clearly seen from Fig. 12, where the water content profiles across the MEA (anode CL and membrane and cathode CL) are plotted for 100 mA/cm^2 at 40 s and 40 mA/cm^2 at 160 s (corresponding to the end of each cold start), respectively. In both cases, ice precipitation in the cathode CL keeps the water content in ionomers constant at the maximum value. Inside the membrane, water diffusion penetrates only one-third of membrane thickness in the case of 100 mA/cm^2 and 40 s, leaving two-thirds of the membrane at the initial water content. In contrast, in the case of 40 mA/cm^2 and 160 s, water diffusion occurs throughout the entire membrane and even increases water content in the anode CL. Clearly, water storage in the membrane differs greatly between these two cases, giving rise to a significant difference in cumulative product water until the cell is shut down.

Membrane thickness effect.— One interesting design parameter to improve cold start is the membrane thickness. While using thicker membranes can increase its water-storage capacity, the product water varies insignificantly between 30 and 45 μm membranes, as shown in Fig. 13. Figure 14 depicts the water-content profiles through the two MEAs, one for a 30 μm membrane and the other for a 45 μm membrane. As seen, the 45 μm membrane is too thick for complete water diffusion at the current density of 40 mA/cm^2 and −20°C. Consequently, the actual amount of water stored in the two membranes remains roughly the same.

Conclusions

A multiphase, multidimensional, and transient model for PEFC cold start has been developed to describe ice formation in dynamic

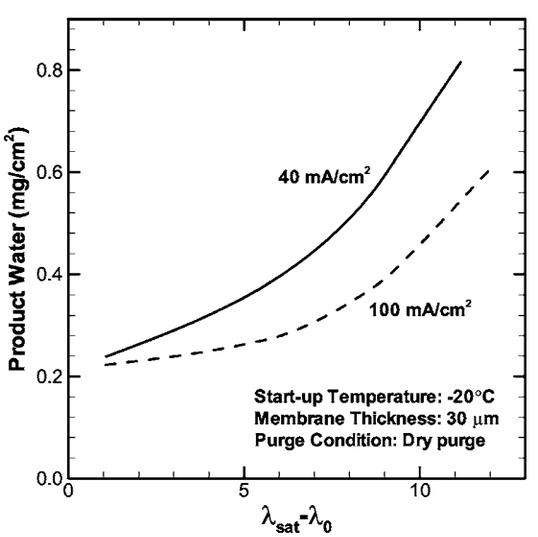

Figure 11. Effect of startup current density on cold-start performance.

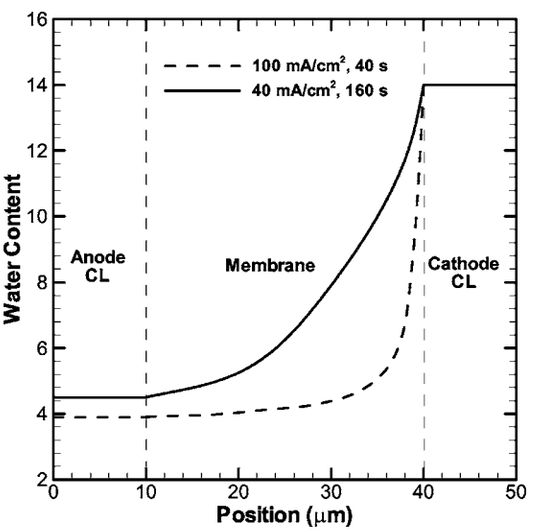

Figure 12. Water-content profiles in the MEA at the end of isothermal cold start under different current densities.

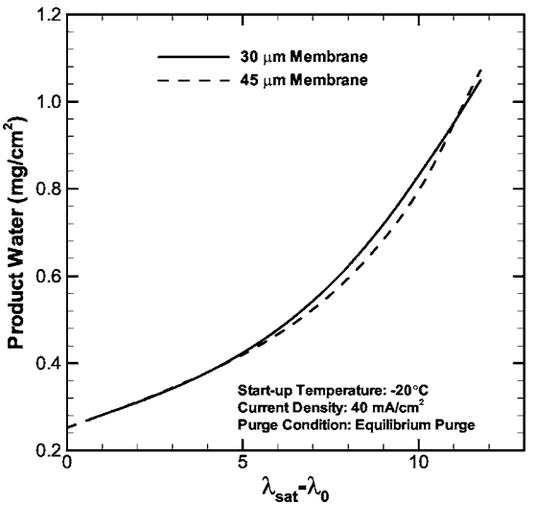

Figure 13. Effect of membrane thickness on cold-start performance.

interaction with water and heat transport as well as ORR. The computational model assumes instantaneous desublimation of water from supersaturated vapor and, in addition, fully incorporates the characteristics of water and proton transport in the membrane at subzero temperatures, heat transfer with phase transition, and electron transport. The computer model is implemented within the commercial flow solver, Fluent, and is amenable to large-mesh, parallel calculations for industrial-scale fuel cells. Cold-start operation of a single cell under constant temperature boundary conditions is simulated. The measured cell-voltage evolution and cumulative product water are predicted reasonably well by the present model. Also, a comparison between the predicted and measured product water is shown for a total of 40 cold-start cases covering a wide range of operation and design conditions, with ±20% accuracy. This lends initial confidence to application of the present model in engineering design and innovation of cold-start strategies.

Full 3D numerical results reveal the profound role of water transport in ice formation in the cathode CL. Furthermore, ice formation impacts ORR and hence shifts the density distribution in the course of startup. The time-evolving current distribution in turn dictates the spatial distribution of heat generation over the entire fuel cell. Thus, the distribution of ice formation or melting depends critically upon multidimensional heat transport over the entire cell. It is striking how the competition of two ORR products, water and waste heat, leads to highly nonlinear and complex dynamics of PEFC cold start. Finally, this multiphase model is applied to forecast the effects of startup current density and membrane thickness on cold-start performance. Dramatic effects of current density are predicted by this model and subsequently verified experimentally.[9] A small difference in cold-start performance between a 30 and a 45 μm membrane is found.

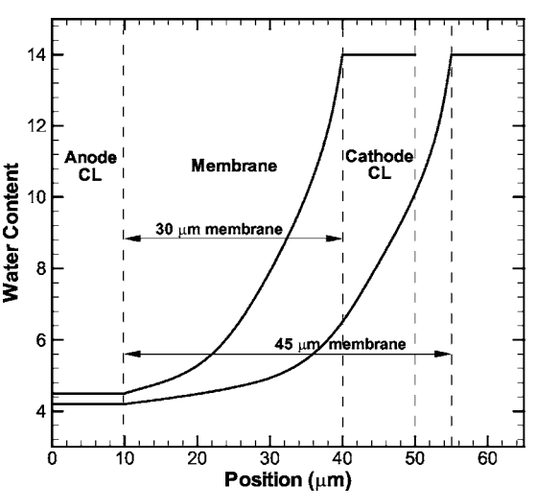

Figure 14. Water-content profiles in the MEA at the end of isothermal cold start with varying membrane thickness (40 mA/cm^2, −20°C, equilibrium purge with 75% RH).

Acknowledgments

This work was supported in part by Penn State Materials Research Institute, Nissan Motor Co., Ltd., and NSF grant no. 0609727. The authors also thank K. Yoshizawa of Nissan for useful discussions.

The Pennsylvania State University assisted in meeting the publication costs of this article

List of Symbols

a	active catalyst area per unit volume, m^{-1}
C^i	molar concentration of species i, mol/m^3
c_p	specific heat, J/kg K
D^i	mass diffusivity of species i, m^2/s
EW	equivalent weight of polymer membrane, kg/mol
F	Faraday's constant, 96487 C/mol
h_{sg}	latent heat of water sublimation, J/mol or kJ/kg
i_o	reference exchange current density, A/m^2
I	current density, A/cm^2
j	transfer current density, A/m^3
M	molecular weight, g/mol
n_d	electro-osmotic drag coefficient
p	pressure, Pa
R	universal gas constant, 8.314 J/mol K
s	ice fraction
t	time, s
T	temperature, K
U_o	thermodynamic equilibrium potential, V
V_{cell}	cell voltage, V

Greek

α	transfer coefficient
η	overpotential, V
ε	porosity
κ	ionic conductivity, S/m
λ	water content in ionomers
ρ	density, kg/m^3
δ	thickness, m

Subscripts

o	initial condition
a	anode
c	cathode
e	electrolyte
CL	catalyst layer
GDL	gas diffusion layer
m	membrane or ionomer
ref	reference
sat	saturation

References

1. R. C. McDonald, C. K. Mittelsteadt, and E. L. Thompson, *Fuel Cells*, **4**, 208 (2004).
2. E. Cho, J. J. Ko, H. Y. Ha, S. A. Hong, K. Y. Lee, T. W. Lim, and I. H. Oh, *J. Electrochem. Soc.*, **150**, A1667 (2003).
3. E. Cho, J. J. Ko, H. Y. Ha, S. A. Hong, K. Y. Lee, T. W. Lim, and I. H. Oh, *J. Electrochem. Soc.*, **151**, A661 (2004).
4. Y. Hishinuma, T. Chikashisa, F. Kagami, and T. Ogawa, *JSME Int. J., Ser. B*, **47**, 235 (2004).
5. M. Oszcipok, D. Riemann, U. Kronenwett, M. Kreideweis, and M. Zedda, *J. Power Sources*, **145**, 407 (2005).
6. M. Oszcipok, M. Zedda, D. Riemann, and D. Geckeler, *J. Power Sources*, **154**, 404 (2006).
7. L. Mao, K. Tajiri, S. Ge, X. G. Yang, and C. Y. Wang, Abstract 998, The Electrochemical Society Meeting Abstracts, Vol. 2005-2 Los Angeles, CA, Oct 16–21, 2005.

8. S. Ge and C. Y. Wang, *Electrochem. Solid-State Lett.*, **9**, A499 (2006).
9. K. Tajiri, Y. Tabuchi, and C. Y. Wang, *J. Electrochem. Soc.*, **154**, B147 (2007); K. Tajiri, Y. Tabuchi, F. Kagami, S. Takahashi, K. Yoshizawa, and C. Y. Wang, *J. Power Sources*, In press.
10. L. Mao and C. Y. Wang, *J. Electrochem. Soc.*, **154**, B139 (2007); L. Mao, Ph.D. Thesis, The Pennsylvania State University, University Park, PA (2006).
11. C. Y. Wang, *Chem. Rev. (Washington, D.C.)*, **104**, 4727 (2004).
12. Y. Wang and C. Y. Wang, *J. Electrochem. Soc.*, **152**, A445 (2005).
13. Z. H. Wang, C. Y. Wang, and K. S. Chen, *J. Power Sources*, **94**, 40 (2001).
14. R. E. Meredith and C. W. Tobias, in *Advances in Electrochemical Science and Engineering 2*, C. W. Tobias, Editor, Interscience Publishers, New York (1962).
15. V. R. Voller, *Numer. Heat Transfer, Part B*, **17**, 155 (1990).
16. Y. Wang and C. Y. Wang, *Electrochim. Acta*, **50**, 1307 (2005).
17. T. E. Springer, T. A. Zawodzinski, and S. Gottesfeld, *J. Electrochem. Soc.*, **138**, 2334 (1991).
18. *Smithsonian Meteorological Tables*, 5th ed., p. 350, Smithsonian Institution, Washington, D.C. (1984).
19. H. Ju, H. Meng, and C. Y. Wang, *Int. J. Heat Mass Transfer*, **48**, 1303 (2005).